Liu, Wenqi; Lian, Junhe; Münstermann, Sebastian; Zeng, Chongyang; Fang, Xiangfan

Prediction of crack formation in the progressive folding of square tubes during dynamic axial crushing

Published in:
International Journal of Mechanical Sciences

DOI:
10.1016/j.ijmecsci.2020.105534

Published: 15/06/2020

Document Version
Peer-reviewed accepted author manuscript, also known as Final accepted manuscript or Post-print

Please cite the original version:
Liu, W., Lian, J., Münstermann, S., Zeng, C., & Fang, X. (2020). Prediction of crack formation in the progressive folding of square tubes during dynamic axial crushing. *International Journal of Mechanical Sciences*, *176*, Article 105534. https://doi.org/10.1016/j.ijmecsci.2020.105534

Prediction of crack formation in the progressive folding of square tubes during dynamic axial crushing

Wenqi Liu[1,2], Junhe Lian[2,3,*], Sebastian Münstermann[1], Chongyang Zeng[4], Xiangfan Fang[4]

[1]Integrity of Materials and Structures, Steel Institute, RWTH Aachen University, Intzestraße 1, 52072 Aachen, Germany

[2]Advanced Manufacturing and Materials, Department of Mechanical Engineering, Aalto University, Puumiehenkuja 3, 02150 Espoo, Finland

[3]Impact and Crashworthiness Lab, Department of Mechanical Engineering, Massachusetts Institute of Technology, 77 Massachusetts Avenue, Cambridge, MA 02139-4307, USA

[4]Institute of Automotive Light Weight Design, University of Siegen, Breite Straße 11, 57076 Siegen, Germany

[*] Corresponding author.

E-mail addresses: junhe.lian@aalto.fi; lianjh@mit.edu

Phone: +358 50 477 0765

Abstract

Experimental and numerical investigations at both lab and structure scales on the plasticity and failure behavior of an automotive dual-phase steel sheet (DP1000) are performed in this study. On the lab level, an extensive experimental program considering the temperature and strain rate effects on the plastic deformation behavior and the stress state dependency of the ductile fracture behavior is designed. On the structure level, dynamic square tube crushing tests are performed on a drop tower. The extended hybrid damage mechanics model is formulated in the study to describe the deformation and damage/fracture behavior of DP1000 considering the influence of temperatures, strain rates, and loading history. The plasticity and fracture description at the lab scale is used to calibrate the material parameters of the model, which is further applied to predict the crashworthiness of the square tube crushing tests. The proposed model has been proven to show very good predictive capability at both lab and structure scales. It is further found that for the modern high-strength steels short cracks could be developed in the tube crushing tests and the crack formation mechanics is shearing and local second-level bending caused by the self-contact between folds.

Keywords

Crashworthiness; Crash box; FEM simulation; Ductile fracture model; Dual-phase steel

1 Introduction

The lightweight concept has become the trend of world automobile development in the last decades. The automotive lightweight design aims to reduce the integral weight of the automobile as much as possible while ensuring the strength and safety performance, thereby improving the dynamic power of the automobile, reducing fuel consumption, and meeting the requirements of environmental protection and energy conservation. In addition to the structural optimization and process improvement, the application of lightweight new materials is the key to achieving automotive lightweight. For instance, the advanced high-strength steels (AHSS) have been intensively developed and mainly used as automotive structural and safety-relevant components (e.g. crash box), etc., due to their attractive combination of strength, formability, and ductility. The crashworthiness property of such structures is their ability to protect the passengers during an impact loading and directly associates with the security of the moving structure. The crash box is an important component to get the good crashworthiness properties for automobiles, especially at the low-speed crash. It is a thin-walled deformable device mounted in between the automobile bumper and the frontal rail. In addition, the introduced groove at a specific position is normally applied to achieve the crush guide design. To obtain better crashworthiness, the design of the crash box in terms of materials, shapes, dimensions, etc. is regularly pursued. The recent studies on the energy absorption and crashworthiness property of thin-walled structures have been reviewed by Fang et al. [1], Baroutaji et al. [2], and Xu et al. [3].

To streamline the analysis of crashworthiness and optimization of the crash box, the mechanical understanding of progressive folding of simple-shaped crash tubes, e.g. circle or prismatic columns, under axial crushing has been well developed since the last decades. The pioneering work was established by Tomasz Wierzbicki and Wlodzimierz Abramowicz in the field of crushing mechanics, where the crushing behavior of the thin-walled structures was investigated analytically [4-6]. The proposed mathematical models considering a basic folding mechanism can predict the mean crushing strength/force, the effective crushing distance, the dissipated energy, and the main features of folds and wrinkles based on the minimum principle plasticity assumption or the rigid-plasticity assumption. The model was further modified by fine-analyzed plastic resistance and collapse mode of a basic folding element, known as the "superfolding elements" [7]. These progressive buckling models considering the static and dynamic loading were validated with experimental investigations on circular and square tubes [8-10].

Since the end of the last century, with the development of the finite element method (FEM), the complex boundary conditions, contact interaction as well as the material elastoplastic constitutive behavior can be taken into account. Wierzbicki et al. [11, 12] firstly combined their superfolding element concept with Abaqus FEM simulation to obtain a detailed analysis of the crush behavior of prismatic rectangular columns. Otubushin [13] also compared the predictive performance of the FEM and analytical model on the mean force and absorbed energy during a drop hammer test on a square mild steel tube. More recently, the FEM is widely applied to analyzing the crashworthiness properties mainly in terms of reflection force and energy absorption of the crash box with various geometries and material properties. For instance, Sun et al. [14] investigated the crashworthiness responses of square aluminum alloy tubes with different thickness types under axial crushing loading. Li et al. [15] compared the crashworthiness of different tubes with functionally graded thickness, tapered uniform thickness, and straight uniform thickness under axial and oblique impact loading, in terms of the specific energy absorption and maximum crushing force. Zhang et al. [16] characterized the bending resistance of a tailor rolled blank top-hat structure under the lateral loading, which has the increased wall thickness in the critical load-bearing areas, and the performance was also compared with the uniform thickness top-hat structure. Bambach et al. [17] compared the numerically predicated energy absorption of crash boxes with different cross-section shapes, i.e. circular, hexagonal, and square. Kohar et al. [18] studied the influence of material mechanical property profiles. i.e. yield stress, ultimate tensile strength, hardening rate, etc., on the component responses including peak force, steady-state crush force, and energy absorption of square tubes under the axial crushing. Gedikli [19] carried out the numerical analyses on the effects of material type (including aluminum alloy and high strength steels), thickness and aspect ratio between the tube length to the diameter of circular tubes. Fu et al. [20] proposed a bionic-bamboo tube microstructure for absorbing energy under axial crushing and designed the shape and number of ribs by FEM to get better energy absorption capacity.

It can be concluded that in most crushing related literature, the main focus has been the correlation of the crashworthiness characteristics, such as energy absorption and mean/peak reflection force, with the geometrical and/or the material information in the recent studies. For this type of studies, only the elastoplastic behavior of the material is concerned, as the crashworthiness characteristic, in particular, the energy absorption is mainly enforced by the plastic behavior of the material. There is a lack of studies focusing on the crack formation mechanics and prediction of the crack formation during the crushing loading. It is notable that the fracture behavior is not critical for the energy absorption devices made by conventional metals, e.g. low-strength aluminum alloys or mild steels, which have very excellent ductility. However, for the modern high-strength steels, their ductile fracture behavior is compromised by the high strength. It shows a complicated dependency on loading conditions. Many recent studies have shown that the loading history and stress state play a significant role in the ductile fracture of modern high-strength metals. Bao and Wierzbicki [21, 22] firstly showed the non-monotonic stress triaxiality effect on the ductile fracture strain, while Bai and Wierzbicki [23] and Xue and Wierzbicki [24] revealed the additional influence of Lode angle on ductile fracture. Marcadet and Mohr [25, 26] studied how the loading path affected the ductile fracture of dual-phase steels. Furthermore, external loading conditions such as temperature and strain rate should also be considered particularly for material behavior under the impact loading [27-31].

To address these findings on the ductile fracture behavior of modern high-strength steels, various material constitutive models have been developed in the last decade. Bai and Wierzbicki firstly formulated the ductile fracture criterion with a general dependency on both stress triaxiality and Lode angle. Alternative fracture criteria are also then further developed by Mohr and Marcadet [32], Stoughton and Yoon [33], Khan and Liu [29], and many more [34-36]. In addition, Bao and Wierzbicki [21] indicated the cut-off value -1/3 on stress triaxiality, below which there will be no fracture occurrence. Lou et al. [37] extended the cut-off value as a function of the stress state. For a comprehensive review and comparison of these models, the readers are referred to these specific papers [38-40]. Alternatively, the coupled damage mechanics models, such as the Gurson–Tvergaard–Needleman (GTN) models [41-43] and the continuum damage mechanics (CDM) models [44] have also been further developed and applied to the high-strength and failure-comprehensive metals [45-47]. Combining the coupled and uncoupled approaches, Lian et al. [48] developed a hybrid damage mechanics model, which introduces a damage initiation concept and the damage induced softening to the original Bai–Wierzbicki uncoupled model [23]. The modified Bai–Wierzbicki (MBW) model offers flexibility to switch between the uncoupled and coupled formulation that reflects the general relation of damage and ductile fracture for engineering materials [49, 50].

Given the various ductile fracture behavior for high-strength steels, especially under various stress states and loading history, it is important to consider the ductile fracture behavior of the prismatic tubes during axial crushing loading either for material selection or the optimization of the crash box geometries. Therefore, the aim of this study is to reveal the crack formation mechanics of progressive folding tubes under axial crushing loading and to develop a model to predict the crack formation. It is emphasized that during the crushing loading, due to the highly non-linear geometrical deformation, the stress state and the deformation history are extremely complicated. Therefore, the main analysis of the crack formation mechanics is focused on the stress state and loading history dependency of the ductile fracture. A dual-phase steel, DP1000 is chosen as the investigated material. The component level crash box test is simplified as the square tube crushing test. The extended hybrid damage mechanics model is presented in this study with both coupled and uncoupled versions, and the effects of stress state, temperature, and strain rate are included in order to accurately predict the plasticity and fracture behavior of the DP1000 steel in the square tube crushing test. The model is introduced in detail in section 2. Section 3 explains the lab-level macroscopic testing program and the component test setup. The material parameter calibration and validation of the damage model are shown in section 4. Finally, section 5 recurs the square tube crushing test with the numerical method and discusses the deformation history and fracture formation mechanics of a square tube during the crushing loading.

2 The extended hybrid damage mechanics model

Following the initial hybrid damage mechanics model by Lian et al. [48], Novokshanov et al. [51] included the temperature and strain rate effects [52] into the yield function of the model for the prediction of the impact toughness of bainitic steel in the Battelle drop weight tear test. Wu et al. [53] enhanced the model for the complex loading conditions (non-proportional loading) with an incremental accumulation rule for the indication of both the damage initiation and final fracture, to predict the ductile fracture of pearlitic-ferritic steel under room temperature and quasi-static loading. In the present study, these two extensions are integrated into one concise and structured formulation and it is also referred to as the extended MBW (eMBW) model.

The yield function of the model is defined by:

$$\varphi_{\mathrm{eMBW}} = \bar{\sigma} - (1 - D) \cdot \sigma_{\mathrm{y}}(\bar{\varepsilon}^{\mathrm{p}},\ \dot{\bar{\varepsilon}}^{\mathrm{p}}) \cdot f(T) \cdot f(\bar{\theta}) \leq 0 \qquad \text{Eq. 1}$$

where $\bar{\sigma}$ is the equivalent stress and D is the damage variable. The rest three terms of the equations are corresponding to the strain hardening and strain rate effect term, the temperature effect term and the Lode-angle-dependent term. The strain hardening and strain rate effect is defined by $\sigma_{\mathrm{y}}(\bar{\varepsilon}^{\mathrm{p}},\ \dot{\bar{\varepsilon}}^{\mathrm{p}})$:

$$\sigma_{\mathrm{y}}(\bar{\varepsilon}^{\mathrm{p}}, \dot{\bar{\varepsilon}}^{\mathrm{p}}) = \sigma_{\mathrm{y}}(\bar{\varepsilon}^{\mathrm{p}}) \cdot \left(1 + c_1^{\dot{\bar{\varepsilon}}} \cdot \ln \frac{\dot{\bar{\varepsilon}}^{\mathrm{p}}}{\dot{\bar{\varepsilon}}_0}\right) \qquad \text{Eq. 2}$$

where $\sigma_{\mathrm{y}}(\bar{\varepsilon}^{\mathrm{p}})$ is referred to as the stress–strain curve under reference strain rate and temperature, while $c_1^{\dot{\bar{\varepsilon}}}$ is the strain rate related parameter; $\dot{\bar{\varepsilon}}^{\mathrm{p}}$ is the equivalent plastic strain rate; and $\dot{\bar{\varepsilon}}_0$ is the reference strain rate, below which the strain effect is not in function. The temperature term $f(T)$ expresses the temperature effect on the yield stress:

$$f(T) = c_1^{\mathrm{T}} \cdot \exp\left(c_2^{\mathrm{T}} \cdot T\right) + c_3^{\mathrm{T}} \qquad \text{Eq. 3}$$

where c_1^{T}, c_2^{T}, and c_3^{T} are the temperature-dependent parameters. Finally, the Lode-angle-dependent term is defined by:

$$f(\bar{\theta}) = c_{\theta}^{\mathrm{s}} + (c_{\theta}^{\mathrm{ax}} - c_{\theta}^{\mathrm{s}}) \cdot \left(\omega - \frac{\omega^{m+1}}{m+1}\right), \qquad \text{Eq. 4}$$

$$c_{\theta}^{\mathrm{ax}} = \begin{cases} c_{\theta}^{\mathrm{t}}, & \bar{\theta} \geq 0 \\ c_{\theta}^{\mathrm{c}}, & \bar{\theta} < 0 \end{cases}, \qquad \omega = \frac{\sqrt{3}}{2 - \sqrt{3}} \left[\sec\left(\frac{\bar{\theta}\pi}{6}\right) - 1\right] \qquad \text{Eq. 5}$$

where $\bar{\theta}$ is the Lode angle parameter, defined by Bai and Wierzbicki [23]; c_{θ}^{s}, c_{θ}^{t}, c_{θ}^{c}, and m are material constants to consider the Lode angle effect on plasticity. The detailed material calibration procedure has been shown in by Lian et al. [48], including its condition to fulfill the convexity requirement. They will not be addressed in this study in detail.

Considering the non-proportional loading condition, the onset of ductile damage initiation (DDI) is controlled by a strain-based locus $\bar{\varepsilon}_{\mathrm{ddi}}^{\mathrm{p}}$ with the dependency on stress triaxiality and Lode angle parameter:

$$\bar{\varepsilon}_{\mathrm{ddi}}^{\mathrm{p}}(\eta_{\mathrm{avg}}, \bar{\theta}_{\mathrm{avg}}) = \begin{cases} +\infty; & \eta \leq \eta_{\mathrm{c}} \\ (D_1 e^{-D_2\eta} - D_3 e^{-D_4\eta})\bar{\theta}^2 + D_3 e^{-D_4\eta}; & \eta > \eta_{\mathrm{c}} \end{cases} \qquad \text{Eq. 6}$$

It is noticed that if the stress triaxiality is lower than a critical value η_{c}, there is no damage or fracture occurrence [21, 53].

Besides, the ductile damage initiation indicator I_{dd} is defined as the integration of accumulated equivalent plastic strain (PEEQ) according to:

$$I_{\mathrm{dd}} = \int_0^{\bar{\varepsilon}^{\mathrm{p}}} \frac{\mathrm{d}\bar{\varepsilon}^{\mathrm{p}}}{\bar{\varepsilon}_{\mathrm{ddi}}^{\mathrm{p}}(\eta_{\mathrm{avg}}, \bar{\theta}_{\mathrm{avg}})} \qquad \text{Eq. 7}$$

The stress and strain at ductile damage initiation are indicated by $\sigma_{\mathrm{ddi}}^{\mathrm{c}}$ and $\bar{\varepsilon}_{\mathrm{ddi}}^{\mathrm{p,c}}$:

$$\sigma_{\mathrm{ddi}}^{\mathrm{c}} = \bar{\sigma}(I_{\mathrm{dd}} = 1), \qquad \bar{\varepsilon}_{\mathrm{ddi}}^{\mathrm{p,c}} = \bar{\varepsilon}^{\mathrm{p}}(I_{\mathrm{dd}} = 1) \qquad \text{Eq. 8}$$

Analogously, the critical equivalent plastic strain $\bar{\varepsilon}_{\mathrm{df}}^{\mathrm{p}}$ for ductile fracture (DF) is defined in Eq. 9 as a strain-based locus as well:

$$\bar{\varepsilon}_{\mathrm{df}}^{\mathrm{p}}(\eta_{\mathrm{avg}}, \bar{\theta}_{\mathrm{avg}}) = \begin{cases} +\infty; & \eta \leq \eta_{\mathrm{c}} \\ (F_1 e^{-F_2\eta} - F_3 e^{-F_4\eta})\bar{\theta}^2 + F_3 e^{-F_4\eta}; & \eta > \eta_{\mathrm{c}} \end{cases} \qquad \text{Eq. 9}$$

The ductile fracture indicator I_{df} is the integration of accumulated equivalent plastic strain from damage initiation to ductile fracture:

$$I_{\mathrm{df}} = \int_{\bar{\varepsilon}_{\mathrm{c}}^{\mathrm{ddi}}}^{\bar{\varepsilon}^{\mathrm{p}}} \frac{\mathrm{d}\bar{\varepsilon}^{\mathrm{p}}}{\bar{\varepsilon}_{\mathrm{df}}^{\mathrm{p}}(\eta_{\mathrm{avg}}, \bar{\theta}_{\mathrm{avg}}) - \bar{\varepsilon}_{\mathrm{ddi}}^{\mathrm{p}}(\eta_{\mathrm{avg}}, \bar{\theta}_{\mathrm{avg}})} \qquad \text{Eq. 10}$$

Finally, depending on the loading process, the damage variable *D* for ductile behavior is summarized as:

$$D = \begin{cases} 0 & \text{for } I_{\mathrm{dd}} < 1 \\ I_{\mathrm{df}} \cdot \frac{\sigma_{\mathrm{ddi}}^{\mathrm{c}}}{G_{\mathrm{f}}} (\bar{\varepsilon}_{\mathrm{df}}^{\mathrm{p}} - \bar{\varepsilon}_{\mathrm{ddi}}^{\mathrm{p}}) & \text{for } I_{\mathrm{dd}} \geq 1 \wedge I_{\mathrm{df}} \leq 1 \\ 1 & \text{for } I_{\mathrm{dd}} \geq 1 \wedge I_{\mathrm{df}} > 1 \end{cases} \qquad \text{Eq. 11}$$

When the ductile damage initiation indicator I_{dd} is smaller than one, the plastic strain is accumulated without damage occurrence. When I_{dd} is equal to one, damage happens, and subsequently, the ductile damage evolution follows an energy-based law, as shown in Eq. 11, where G_{f} stands for the energy which is dissipated by a material point between damage initiation and fracture. When the ductile fracture indicator I_{df} is larger than one, the damage variable D is assigned as one, final fracture happens on the material point, and the material completely loses its load-carrying capability.

The coupled and uncoupled formulation can be easily switched in the eMBW model according to the different behavior of materials and applications. Lian et al. [54] compared the damage behavior of two steel grades, DP600 and high-strength low-alloyed steel, and completely different damage behavior was simulated by switching the MBW models from coupled to uncoupled formations. By setting the damage initiation strain function the same as the ductile fracture one, the model can be easily transferred into an uncoupled model. In this case, once the damage initiation or ductile fracture indicator reached one, the final fracture occurs. During the whole deformation process, no damage will be accumulated and introduced to the yield function. In the present study, the uncoupled formulation of the eMBW model is employed due to the late damage initiation and rapid damage evolution to fracture of the material [55]. The detailed model parameter calibration and validation are shown in section 4.

3 Material and experiments

In this study, a dual-phase sheet steel (DP1000) with a thickness of 1.5 mm is selected. It is composed of ferrite and martensite phases and the phase fraction of martensite is about 45%. The detailed microstructural information can be found in Liu, et al. [56].

3.1 Lab-level experiments

To determine the material mechanical properties, a comprehensive experimental program considering material plasticity and fracture behavior under variable temperatures and loading conditions is designed and carried out in this study:

- Uniaxial tensile test at room temperature (RT, 25 °C) and quasi-static (QS, 0.0001 s^{-1}) loading to obtain the plastic-hardening characteristics under uniaxial tension;
- Uniaxial tensile tests at different temperatures (-40 °C, 25 °C, 100 °C) and different strain rates (from QS to high strain rates, 0.0001 s^{-1}, 0.001 s^{-1}, 0.01 s^{-1}, 0.1 s^{-1}, and 100 s^{-1}) to obtain the plasticity description of the material response at different temperatures and strain rates;
- Damage/fracture tests with various sample geometries (central-hole tension, notched dog-bone tension, plane-strain tension, and shear tests) at RT and QS to characterize the damage/fracture behavior of the material in a broad range of stress states;

Based on the fracture specimen geometry design proposed in [55], all uniaxial tensile tests are performed and evaluated according to EN ISO 6892-1:2016 [57] on the specimens with the consistent dog-bone outline, as shown in Fig. 1. The specimens are smooth dog-bone specimen (SDB), central-hole specimen with the hole diameter 6 mm (CHD6), notched-dog-bone specimens with the notch radius 50 mm (NDBR50), plane-strain specimens with the out-of-plane notch radius 2 mm and 16 mm (PSR2, PSR16), and shear specimen (SH) with the rounded eccentrically positioned in-plane notches. In our previous study [55], the detailed design of the geometry has been optimized to achieve locally proportional loading conditions at the crack initiation spot, which is important for both the fracture parameter calibration and the damage mechanism identification at various stress states. All tests are along the material rolling direction (RD).

The tests under the strain rate of 0.1 s^{-1} are executed on a 100 kN multi-functional testing machine manufactured by Zwick/Roll. The applied load and extension are measured by means of a load cell and optical extensometer, respectively. Besides, the adiabatic temperature increase during plastic deformation is also measured for tests under intermediate loading conditions. The high-resolution thermal camera VarioCAM (InfraTec GmbH, Germany) assists in the adiabatic heating analysis for the uniaxial SDB tensile tests. The camera set-up is controlled by the IRBIS software remote 3.0 (InfraTec GmbH, Germany). The camera detector is an uncooled microbolometer focal plane array consisting of an arrangement of 640 - 480 elements gathering longwave infrared radiation from 7.5 μm to 14 μm. The temperature sensitivity of the thermal camera is better than 0.05 K at 303 K. The device recorded pictures at a detection rate of 50 Hz during experiments. During the tensile tests, the thermal camera can monitor the temperature changes on the surfaces of the specimens to characterize the adiabatic heating effects of the specimens at different strain rates quantitatively. The tensile tests at 100 s^{-1} are carried out on a 50 kN testing machine with a servo-hydraulic system HTM 5020 from Zwick/Roll. Instead of the optical extensometers, the specimen displacement during deformation is measured by a digital image correlation (DIC) system. The DIC system includes two high-speed SA5 Photron cameras and the image capturing and post-processing software (ARAMIS). The detailed set-up of the high strain rate testing including the specimen geometry is found in Fang and Grams [58]. The thermal camera measurement is not available during the tests at the strain rate of 100 s^{-1}. At least three parallel tests are carried out for each tensile test condition.

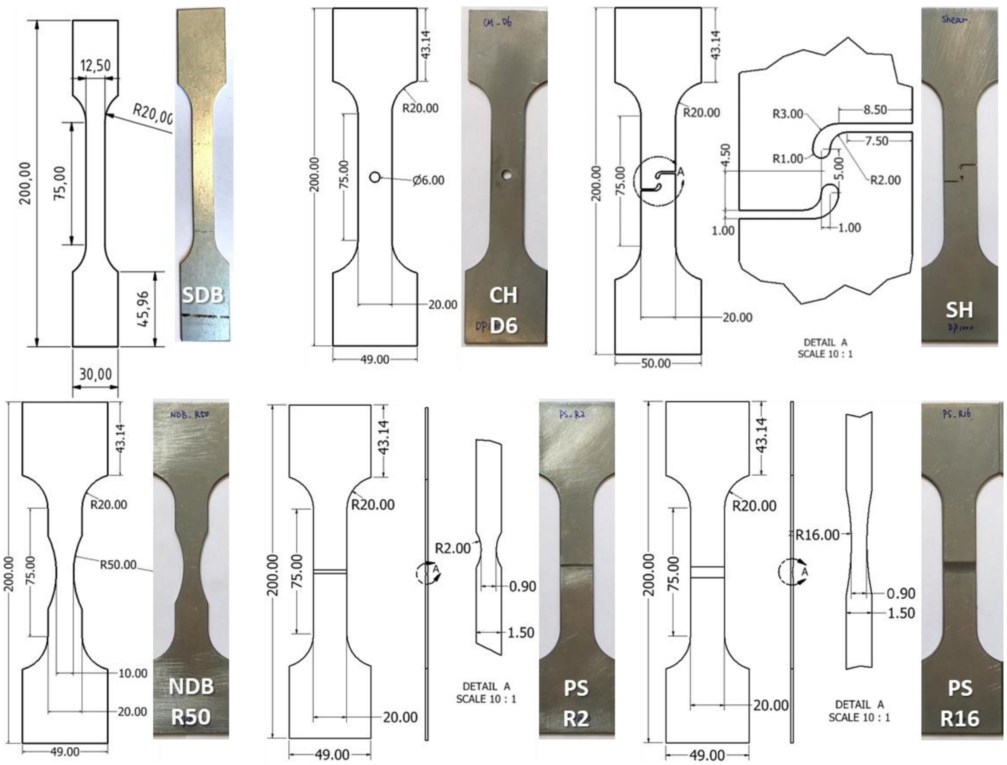

Fig. 1 The geometry details of the lab-level tests.

3.2 Component-level experiments

The crash box investigated in this study is a laser-welded prismatic profile with a square cross-section. The component is firstly manufactured by a pre-bending process of a flat sheet to obtain the prismatic structure in a U shape. Two pieces of the pre-bending samples are then welded together, and the laser-welded seams locate in the middle of the two opposite sidewalls, as shown in Fig. 2. In addition, to ensure a stable and regular folding process during the impact loading, two rectangular indentations are introduced at the top part of the opposite side walls without any weld seams. Fig. 2 shows a photo and a drawing for specimen geometry including the detailed dimensions. This geometry of a simplified square tube is a convenient surrogate for a real crash box component and suitable to validate the envisaged improvement of the crash performance, the test is named as the square tube crushing test.

The dynamic loading is carried out by a drop weight tower device with the loading axis parallel to the RD. The applied energy is about 10 kJ with a drop mass of 129.5 kg and a drop height of 8 m. The temporal evolution of force and displacement of the impactor during the tests are measured by load cells and the laser triangulation system, respectively. In addition, the test is also recorded with a high-speed camera system (5000 frames/s) for monitoring the folding evolution.

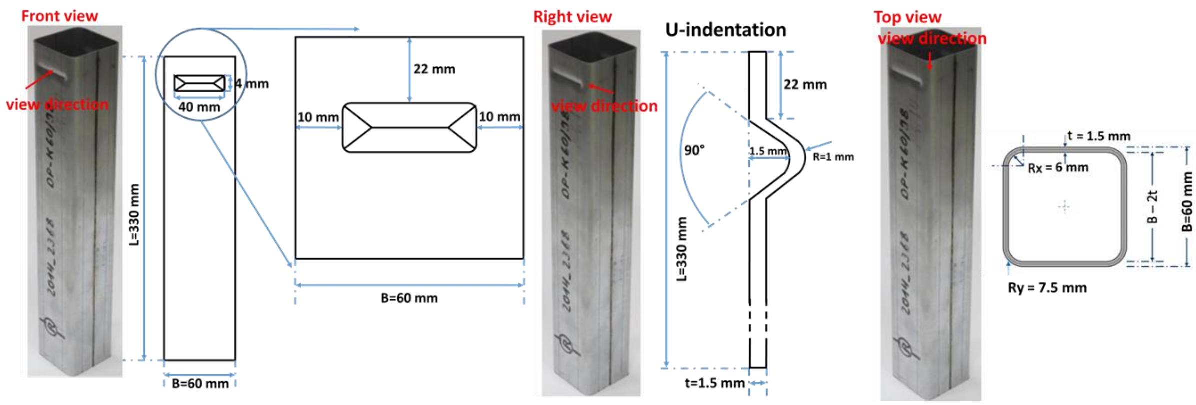

Fig. 2 DP1000 square tube crushing test specimen photo and schematic drawing for specimen geometry with detailed dimensions. (There are symmetrical two indentations on the profile opposite surfaces with the same geometry.)

4 Model parameter calibration and validation

The study is providing a clear and detailed parameter calibration procedure for the description of both the plasticity and fracture behavior of the material. The plasticity description, as shown in the experimental part, includes the flow response of the material under RT and QS condition, and its responses under different temperatures and strain rates. For the derivation of the strain rate effects, a special effort is made to derive firstly the isothermal response with the help of temperature data measured by the thermal camera instead of directly using the constant adiabatic responses widely used in the literature. In addition, by using the temperature data, a new method to calibrate the Taylor-Quinney coefficient change from quasistatic to adiabatic condition is proposed, with which the corresponding description is directly identified instead of inversely fitted. The overall method for the plasticity description is complete and transferable for other materials.

For the failure description of the material, the main concern is the stress state and loading history dependency, as the aim is to understand the crack formation mechanisms in the square tube crushing test, in which very complicated stress states are involved during the folding and crushing processes. Above it, the deformation history of the local material point is adding another level of complexity, demonstrating a dramatic change of its stress state, e.g. from uniaxial compression to shearing and finally to plane-strain tension. Therefore, to capture the effect of stress state and its evolution on the ductile fracture is the primary objective to tackle the crack initiation simulation in the complex component-level test. As the loading is dynamic, one could expect the strain rate would also affect the ductile fracture behavior. Due to the complexity to conduct these experiments and especially to realize a *constant strain rate* loading history, which is still a wide-open challenge in the state of the art, this effect is not considered in the current study. Besides, for understanding the mechanics of crack formation in the crushing test, it is rather a secondary effect.

Before the ductile fracture parameters are used in the tube crushing test simulation, their performance is also validated in the lab scale by comparing the global force–displacement responses for various stress states and the failure pattern of specimens between the numerical simulation and the experiments.

4.1 Elasto-plastic parameters

For the uncoupled eMBW model, the material parameter calibration procedure follows the aforementioned material deformation stages in section 2. First of all, the loaded steel undergoes the linear-elastic deformation stage. It is governed by Hook's law, and a constant Young's modulus E typically equal to 210 GPa is applied for steels. For the plasticity description, the response under QS and RT is firstly calibrated. Then by using the tensile tests conducted under QS at different temperatures, the temperature effect is described. The third step is to use the tensile data conducted at RT but various strain rates and the temperature data measured by the thermal camera to calibrate the strain rate effects.

4.1.1 Flow curve identification at RT and QS condition

The flow curve of plastic deformation is derived from the smooth tensile test at room temperature and quasi-static loading conditions in the formulation of the combined Swift and Voce law (Eq. 12). The calibration procedure is shown in our previous study [55] and therefore it is not repeated here. The final calibrated hardening parameters are listed in the first two rows in Table 2, and the flow curve is presented in Fig. 3.

$$\bar{\sigma}_{\mathrm{y}}^{\mathrm{S-V}}(\bar{\varepsilon}^{\mathrm{p}}) = \alpha \cdot A(\bar{\varepsilon}_0 + \bar{\varepsilon}^{\mathrm{p}})^{\,n} + (1-\alpha) \cdot [k_0 + Q(1 - e^{-\beta_0 \bar{\varepsilon}^{\mathrm{p}}})] \qquad \text{Eq. 12}$$

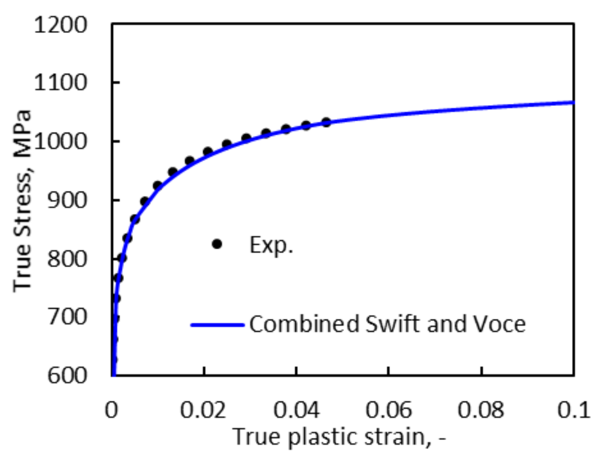

Fig. 3 Experimental and the extrapolated flow curves according to the combined Swift–Voce law.

4.1.2 Temperature sensitivity parameters identification

For the temperature sensitivity parameter calibration, the stress–strain response at RT and QS is assumed as reference. The stresses at the true plastic strain of 0.01 are used to evaluate the temperature effects, as shown in Fig. 4 (a). As the adiabatic heating is not effective for QS tests, the temperature sensitivity is calibrated directly based on these data. The fitting result for temperature dependence is shown in Fig. 4 (b) and the temperature sensitivity parameters are listed in Table 2.

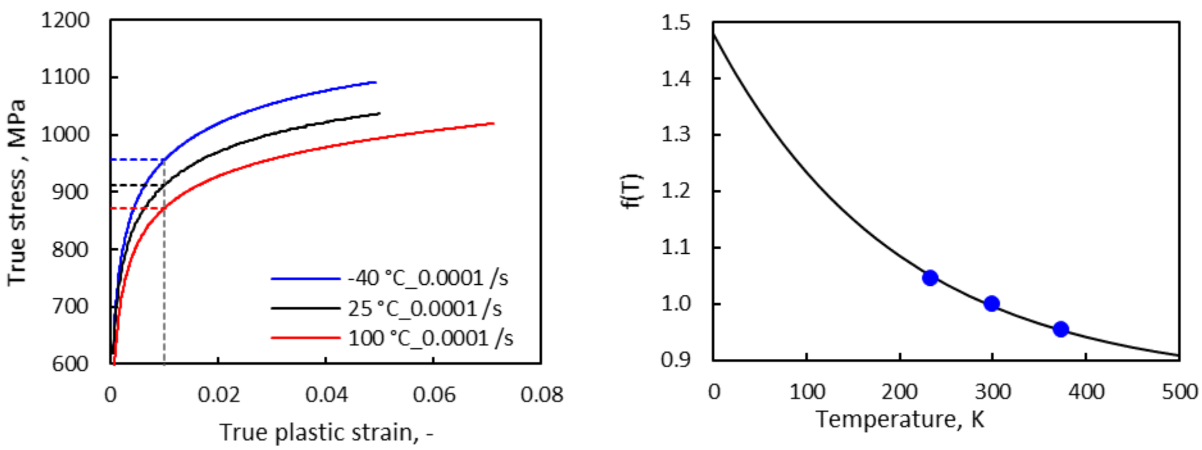

(a) (b)

Fig. 4 Temperature dependence of DP1000. (a) Flow curves at different temperatures; (b) Temperature dependence fitting.

4.1.3 Strain rate sensitivity parameters identification

For loading rates above the QS condition, the temperature increase is activated during plastic deformation. To calculate the strain rate effect based on the isothermal assumption, the stress–strain response shall be corrected first. The following general procedure is proposed to conduct the correction and parameter fitting:

1. Uniaxial tensile tests of SDB specimens under quasi-static and variable temperatures are carried out to obtain the temperature dependence $f(T)$ for the reference material.
2. Uniaxial tensile tests of SDB specimens from quasi-static to intermediate strain rates (0.001 s^{-1}, 0.01 s^{-1}, 0.1 s^{-1}) combined with the infrared confocal thermal camera for the measurement of the temperature increase ΔT of specimens under adiabatic heating conditions.

3. Calculate the instantaneous $f(T)$ with the measured ΔT during the plastic deformation and then automatically to get the isothermal stress–stress response according to Eq. 13.
4. Fit the strain rate sensitivity parameters with the data from the isothermal stress–strain curves according to Eq. 2.

$$\sigma_{\text{adi}} = f(T) \cdot \sigma_{\text{iso}} \qquad \text{Eq. 13}$$

For the tests under intermediate strain rates with thermal camera measurements, the adiabatic heating correction can be achieved with step 1 and 2. Step 1 has already been conducted and shown in Fig. 4. For step 2, Fig. 5 displays an example for the measured temperature field from the thermal camera during the 0.1 s^{-1} uniaxial tensile test. It is clear that before necking ($\bar{\varepsilon}^{\text{p}} \cong 0.05$), the temperature distribution within the uniform deformation zone is in general homogeneous. The average temperature value in a pre-defined uniform deformation zone is calculated to indicate the temperature increase ΔT with plastic deformation, shown as dashed lines in Fig. 6 (a). Combining $f(T)$ from Eq. 3 with the measured adiabatic flow curves (solid lines in Fig. 6 (a)) and Eq. 13, isothermal flow curves can be calculated directly, shown as round dot lines in Fig. 6 (a). Finally, the strain rate sensitivity can be calibrated in this measured strain rate range based on step 4. The logarithm function in Eq. 2 is fitted based on the isothermal flow stresses at the true plastic strain equal at 0.01. The fitting result for strain rate dependence is shown in Fig. 6 (c) and the strain rate sensitivity parameters are listed in Table 2.

Furthermore, for the high strain rate tests without thermal camera measurements, the adiabatic heating correction in step 3 shall be achieved based on a series of theoretical equations and classical coefficients. The calculation principle is based on the conservation of energy from plastic work to heat assuming a certain fraction of the plastic work is released to the environment, as shown in Eq. 14:

$$\Delta T = T - T_0 = \int_0^{\varepsilon} \frac{\beta}{\rho \cdot C_{\text{P}}} \sigma_{\text{iso}} \cdot \mathrm{d}\varepsilon \qquad \text{Eq. 14}$$

where ΔT represents the temperature rise in the specimen during the adiabatic heating; T and T_0 are the instantaneous temperature and the reference temperature, respectively. The two parameters ρ and C_{P} are material density and specific heat capacity. The fraction β is referred to as the Taylor–Quinney Quinney coefficient [59, 60]. For the QS condition, the Taylor–Quinney coefficient β is considered as zero and for very high strain rates, where the complete adiabatic hearing condition is fulfilled, the Taylor–Quinney coefficient β is often assumed to be 0.9 for metals. However, for the intermediate strain rates, the transition from QS to adiabatic condition, the Taylor–Quinney coefficient β needs to be calibrated. In the following, an approach is proposed to calibrate the Taylor–Quinney coefficient β during the transition range of strain rates. Assuming both of material constants and the Taylor–Quinney coefficient β keep constant during the plastic deformation, Eq. 14 can be transferred to the following:

$$\Delta T = \frac{\beta}{\rho \cdot C_{\mathrm{P}}} \int_{0}^{\varepsilon} \sigma_{\mathrm{iso}} \cdot \mathrm{d}\varepsilon \qquad \text{Eq. 15}$$

Therefore, with the measured data of the temperature rise by the thermal camera, the Taylor–Quinney coefficient β can be calculated by the following equation.

$$\beta = \frac{\rho \cdot C_{\mathrm{P}} \cdot \Delta T}{\int_{0}^{\varepsilon} \sigma_{\mathrm{iso}} \cdot \mathrm{d}\varepsilon} \qquad \text{Eq. 16}$$

The calculated Taylor–Quinney coefficient β for the corresponding higher strain rates are shown as the red points in Fig. 6 (b). It is clearly seen that the tested strain rates are all in the transition range, between zero and 0.9. This also emphasizes that the proposed method to calibrate the strain rate sensitivity is proper, as assuming the Taylor–Quinney coefficient β to 0.9 for these cases will overestimate the thermal softening effect to the material, leading, therefore, incorrect strain rate sensitivity. With these data and taking the β as zero at QS loading and 0.9 at higher strain rates, e.g. 1000 s^{-1}, the isothermal-adiabatic transition curve is fitted according to Eq. 17, as shown in Fig. 6 (b). The β value at higher strain rates is regarded as β_{i} in the equation, and S_{c} and $\dot{\varepsilon}_{\mathrm{c}}$ are the fitting parameters as listed in Table 2.

$$\beta = \frac{\beta_{\mathrm{i}}}{2}\left\{1 + \tanh\left[S_{\mathrm{c}} \cdot \log\left(\frac{\dot{\varepsilon}}{\dot{\varepsilon}_{\mathrm{c}}}\right)\right]\right\} \qquad \text{Eq. 17}$$

The employed transition equation gives a smooth transition and reaches a good quality to represent the input data with a coefficient of determination R^2 of 0.91. It is noted that among the three parallel tensile tests, only one test is companied with thermal camera measurement. Therefore, there is only one series of temperature increase – strain data for each strain rate. The deviation on the 0.001 s^{-1} might be minimized by more parallel thermal camera measurements to get better fitting quality on the Taylor–Quinney coefficient. For high strain rate tests without thermal camera measurement, the Taylor–Quinney coefficient can be calculated according to Eq. 17 and for 100 s^{-1}, $\beta_{100} = 0.89$. Then the isothermal flow curves can be calibrated by combing Eqs. 3, 13 and 16. The calculated temperature increase and isothermal flow curve are also added in Fig. 6 (a). The average flow stress with error bars under 100 s^{-1} at $\varepsilon_{\mathrm{t,p=0.01}}$ is also added to validate the strain rate dependence curve in Fig. 6 (c). It is illustrated that the fitted strain rate sensitivity from the intermediate strain rate range is still appropriate for a higher strain rate.

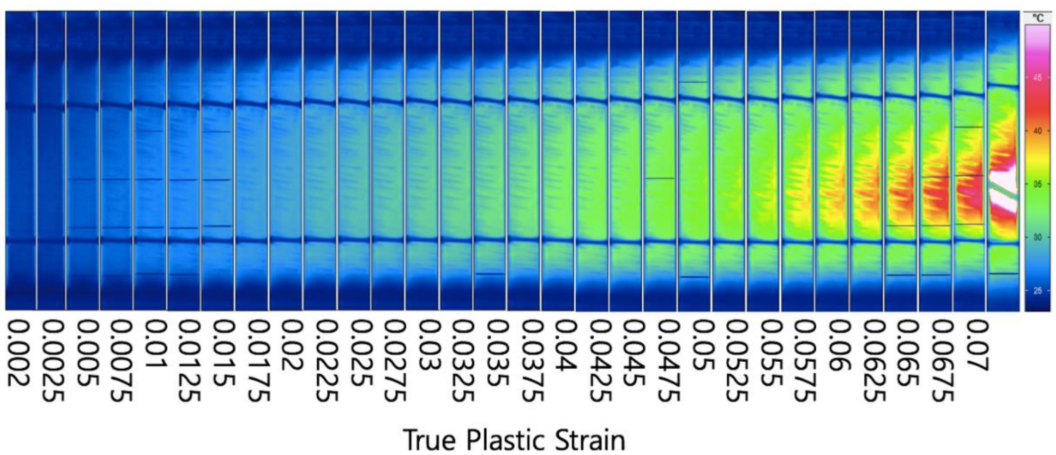

Fig. 5 Temperature field of the uniaxial tensile test at the strain rate of 0.1 s^{-1}.

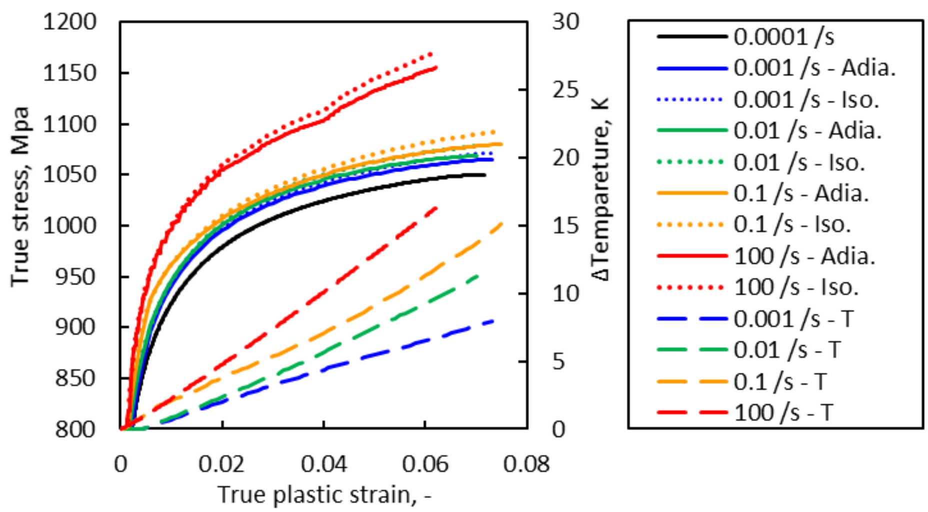

(a)

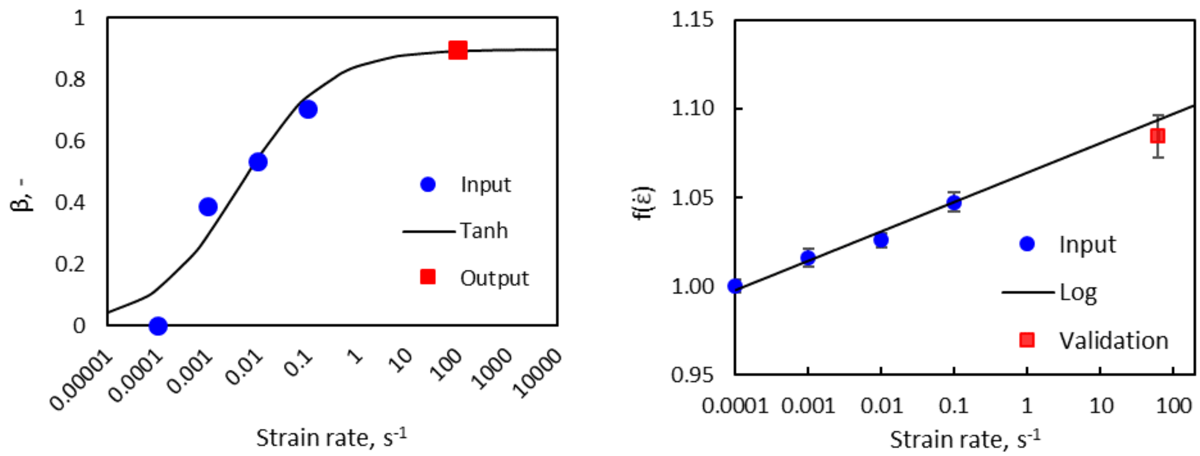

(b) (c)

Fig. 6 Adiabatic heating correction and strain rate dependence of DP1000. (a) Adiabatic and isothermal flow curves at different strain rates with measured temperature increase; (b) The Taylor–Quinney coefficient β as the function of strain rate; (c) Strain rate dependence fitting.

4.2 Ductile fracture parameters

The damage and fracture parameters are determined using a hybrid experimental and numerical method, i.e. inverse fitting by comparing and numerical simulation by finite element simulation with the experimental results based on at RT and QS (crosshead velocity of 0.2 mm/min) loading condition.

The corresponding finite element models are constructed in the commercial FE code Abaqus/Explicit with respect to the specimen geometries. For sheet steels, a 3D model corresponding to the half-thickness of the sample is built, as presented in Fig. 7. It is noted that this is different from our previous study [55] for the sample geometry optimization, where 1/8 model is used due to the sample and loading symmetry. Here, as the aim is also to predict the crack initiation and propagation, where the in-plane symmetry is lost, the 1/2 model is a proper choice. One can also notice that only the part of the sample within the measurement of the extensometer is modeled, as the displacement is measured within this length, and force is only concentrated around the notch region. During the deformation, the nodes on z symmetrical plane are basically restricted to moving in the z-direction, the bottom surface is assigned with the full constraint boundary condition, while a constant velocity is applied to the nodes on the top of the model.

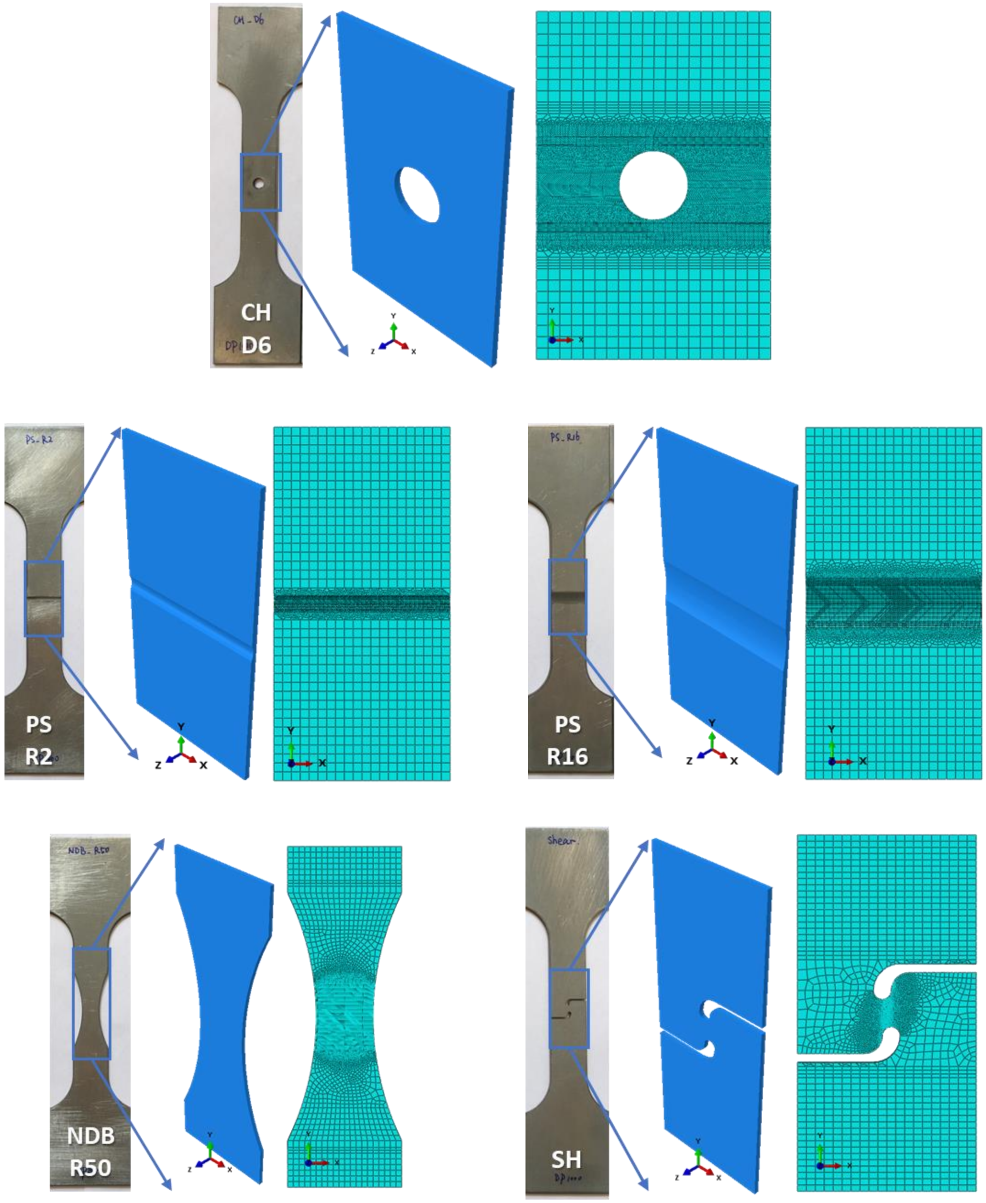

Fig. 7 FE model setup for CHD6, PSR2, PSR16, NDBR50, and SH.

As the mesh is a key factor influencing the FE simulation, especially damage mechanics simulations, in this study, a consistent element type and size at the critical plastic deformation zone across all the models are employed to avoid any severe impact of the mesh size. In the critical deformation area, fine (0.1 mm × 0.1 mm × 0.1 mm), regular 3D brick elements with reduced integration (C3D8R) are used to get a reliable result based on the length scale of the cracks, while the rest part of the model features a coarser mesh to save calculation time.

With the extrapolated flow curve and FE model, a von Mises plasticity model is employed firstly to simulate the material response only with the plasticity deformation. Fig. 9 displays the experimental and numerical simulation comparison on the globe force–displacement curves of all fracture tests. The experimental data is plotted as a red band to include all parallel tests' results. The von Mises simulation results are indicated by blue solid lines. Comparing experiments and von Mises simulation after the maximum force at certain displacement, a distinct deviation between the experimental and numerical results can be observed. In terms of the investigated steel DP1000, for most stress states, the deviation occurs right before the sudden load drop, especially for the shear and plane-strain loading, which indicates the faint damage-induced softening for this grade of DP1000. Hence, the uncoupled damage model can be employed, in which the ductile damage initiation is the same as the ductile fracture in the eMBW model.

Accordingly, in simulation, the local stress and strain variables are analyzed on the critical elements identified by the metallographic analysis at the crack initiation spot [55]. By analyzing the average stress state variables, i.e. stress triaxiality and Lode angle parameter until DF and the critical equivalent plastic strain at DF moment for all fracture specimens, as listed in Table 1, the ductile fracture locus (DFL) can be fitted according to Eq. 9 and presented in Fig. 8. It is demonstrated that the designed specimen geometries achieve the aimed stress states, and the comment stress states range is covered by a series of consistent uniaxial tensile tests in the parameter calibration process.

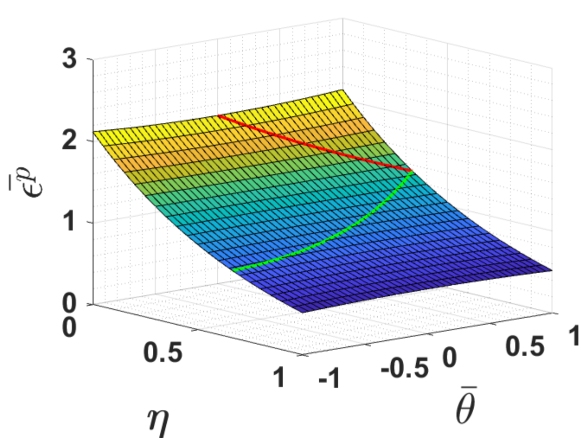

Fig. 8 Ductile fracture locus of DP1000.

Table 1 Stress state parameters and critical equivalent plastic strain for ductile fracture of interested stress states.

	Lode angle parameter $\bar{\theta}$	Stress triaxiality η	PEEQ at DF
CHD6	0.93	0.49	1.03
NDBR50	0.48	0.60	0.90
PSR2	0.02	0.89	0.63
PSR16	0.02	0.75	0.76
SH	-0.01	0.02	1.97

Table 2 Calibrated parameters of DP1000 in the eMBW model.

Notation	Value	Comments and equations
A	1300 (MPa)	Swift law parameter (Eq. 12)
$\bar{\varepsilon}_0$	$2.3e^{-14}$	Swift law parameter (Eq. 12)
n	0.075	Swift law parameter (Eq. 12)
k_0	773.28 (MPa)	Voce law parameter (Eq. 12)
Q	266.19 (MPa)	Voce law parameter (Eq. 12)
β_0	73.94	Voce law parameter (Eq. 12)
α	0.5	Hardening law weight (Eq. 12)
E	210 (GPa)	Elastic modulus
μ	0.3	Poisson Ratio
c_{θ}^{s}	1.0	Stress state corrector (Eq. 4)
c_{θ}^{t}	1.0	Stress state corrector (Eq. 5)
c_{θ}^{c}	1.0	Stress state corrector (Eq. 5)
m	0.0	Stress state corrector (Eq. 4)
C_1^{T}	0.62	Temperature effects (Eq. 3)
C_2^{T}	0.0050	Temperature effects (Eq. 3)
C_3^{T}	0.86	Temperature effects (Eq. 3)
$C_1^{\dot{\bar{\varepsilon}}}$	0.007	Strain rate effects (Eq. 2)
ρ	7870 $(\mathrm{kg/m^3})$	Density (Eps 14 and 15)
C_{P}	466 $[\mathrm{J/(kg \cdot K)}]$	Specific heat capacity (Eps 14 and 15)
β_{i}	0.9	Specific heat fraction parameter (Eq. 16)

S_{c}	0.58	Specific heat fraction parameter (Eq. 16)
$\dot{\varepsilon}_{\mathrm{c}}$	0.0043 (s^{-1})	Specific heat fraction parameter (Eq. 16)
F_1	2.12	Ductile fracture parameter (Eq. 9)
F_2	1.41	Ductile fracture parameter (Eq. 9)
F_3	2.06	Ductile fracture parameter (Eq. 9)
F_4	1.32	Ductile fracture parameter (Eq. 9)

4.3 Model validation

For the validation of the model as well as the calibrated fracture parameters, the simulation with the eMBW model has been run and the crack imitation and propagation are realized by element deletion. The force–displacement responses of all the geometries are shown in Fig. 9. Overall, comparing with the experimental force–displacement curves, the mechanical properties including plastic deformation and ductile fracture behavior of DP1000 are well described in the eMBW simulation (indicated by black dash lines). In addition, the final fracture pattern of various geometries is also used to validate the model prediction, as shown in Fig. 10. In terms of the local strain patterns, the model also captures the localization behavior and the final fracture tendencies of all fracture specimens in experiments reasonably. Two shear bands are observed in simulation on the central-hole and notched-dog-bone specimens' surfaces, and the final fracture occurs along one of the shear bands. The slant fracture propagation is well captured by the eMBW model for CHD6 and NDBR50. While in plane-strain specimens, both strain localization and final fracture happen at the minimum thickness position along the through-thickness plane. For the shear specimen, the strain localization is in the area between the two rounded eccentrically positioned in-plane notches. An external point forms on each notch edge with the increased plastic deformation, and the final fracture on the SH specimen takes place along the line connecting these two sharp points.

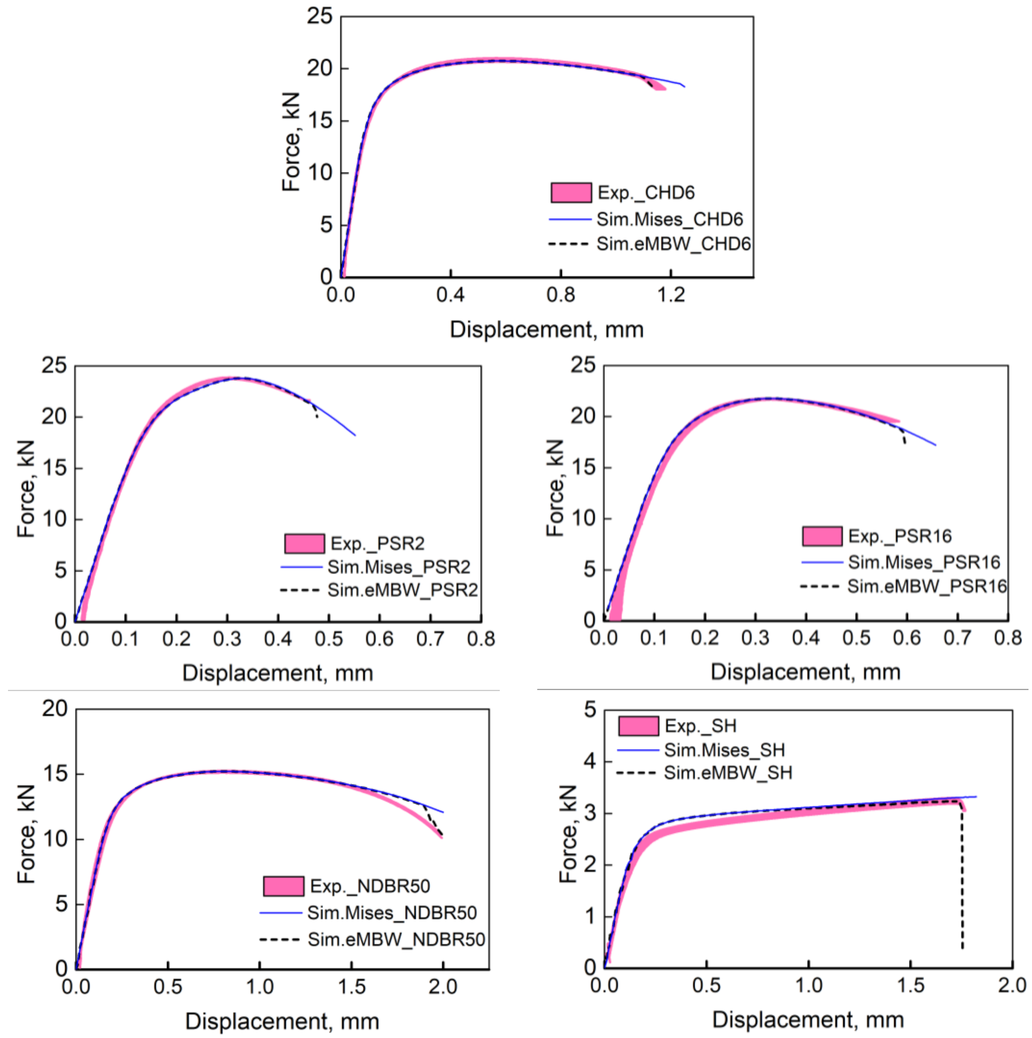

Fig. 9 Experimental and numerical simulation comparison on force–displacement responses of CHD6, PSR2, PSR16, NDBR50, and SH fracture tensile tests.

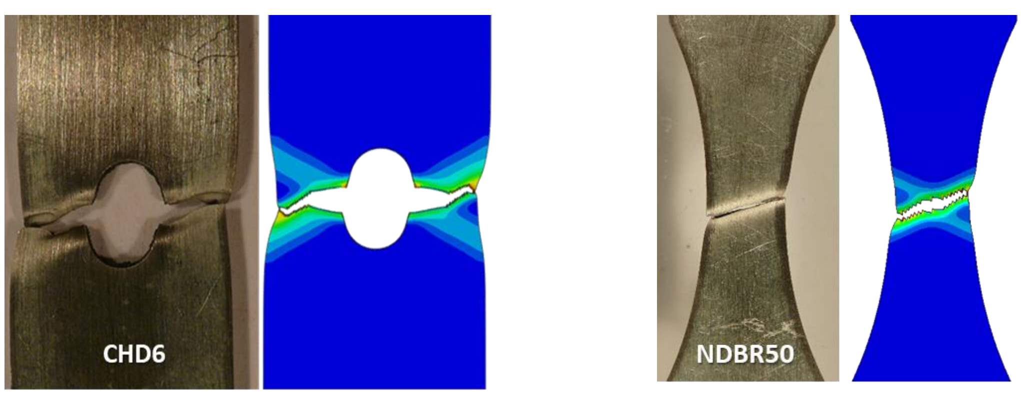

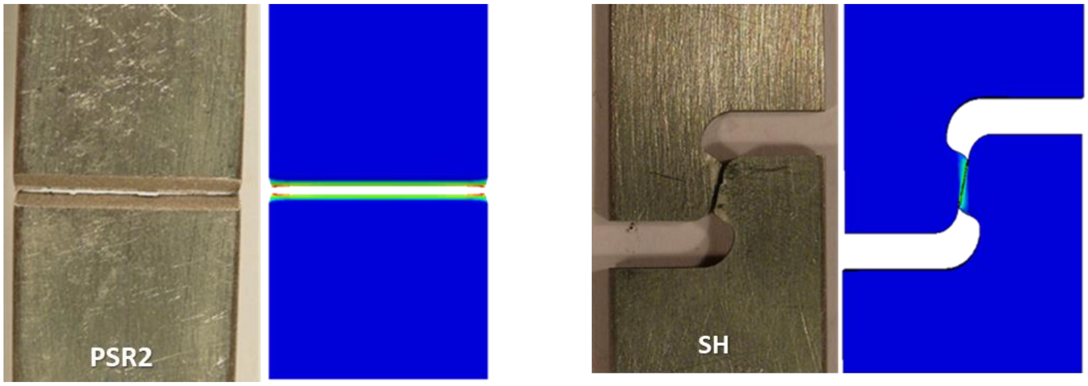

Fig. 10 Experimental and eMBW model simulation comparison on fracture pattern of CHD6, NDBR50, PSR2, and SH specimens.

5 Model application to the square tube crushing test

5.1 FE model setup

Abaqus/Explicit is employed as the FE solver in this application. The FE model for the square tube crushing test is built up according to the experimental profile geometry and test condition given in section 3, as shown in Fig. 11, including the assembly, loading condition, and mesh settings. As aforementioned, the square tube is tested under axial loading in a drop weight device, while in numeral simulation, the assembly of the tube crushing model contains two parts except for the deformable specimen, a rigid body plate is also defined to reproduce the crushing test conditions. It is used to represent the impact hammer in the test and contacts the specimen top surface through a reference point at the plate center. Besides, it is assigned with the drop mass (129.5 kg) and predefined initial impact velocity (12.52 m/s) at the reference point. The specimen bottom surface deformation is constrained in all degrees of freedom, i.e. encastre, in order to fix the profile during impact. Furthermore, a general contact relationship is chosen for the whole model to prevent penetration between the hammer and deformable specimen as well as the intersection between the individual elements during the deformation process. In the end, the frictionless mode is chosen.

In the deformable part, a one-quarter profile geometry is set up with a 3D FE model containing the C3D8R elements to improve the calculation performance. Based on the experimentally deformed profile, it is demonstrated that the deformation mainly happens in the longitudinal distance until 160 mm, and the critical fracture zone always locates at the bending corner of the profile, as indicated in experimental results in Fig. 12 (c). Therefore, the pre-bending corner area along the length until 160 mm is treated as the critical deformation zone, marked as the red area in Fig. 11 (b). In this area, the minimum mesh size is 0.3 mm × 0.3 mm × 0.5 mm (i.e. three elements along thickness direction). In addition, the left uncritical zones are meshed with a homogenized element size of 1 mm × 1 mm × 0.5 mm. This element size is still much large than the one used in the lab-scale simulation, and therefore, this mismatch could probably overlook the strain gradient effect. However, as the total element number has ready reached about quarter-million and we are dealing with a complicated impact loading with contact, the current model already causes more than 1000 CPU hours on a modern workstation. In addition, although a damage mechanics model is generally employed, due to its uncoupled formulation, the mesh effect has also been downsized compared to a completely coupled version. Finally, the rectangular pre-indentation part is also introduced in the FE model to ensure the deformation in simulation as required.

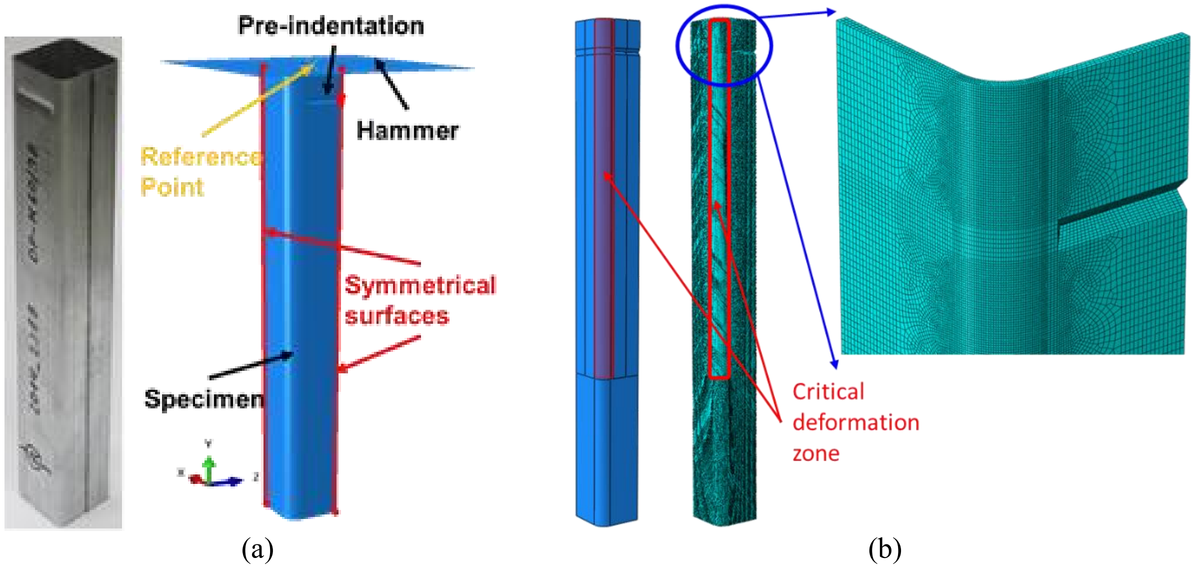

Fig. 11 Square tube crushing test simulation set up. (a) Experimental profile before impact and FE model assembly; (b) FE model mesh setting.

5.2 Results

The results comparison between experiments and simulation is shown in Fig. 12. When the simulation starts, the impact hammer impinges the deformable profile and induces deformation in the profile until all impact energy has been absorbed or dissipated. Then a spring back process is observed in both experiments and simulation. Generally, with the one-quarter FE and eMBW model simulation, the recurrence of crash box material behavior including the force–displacement response, total impact energy absorption, globe deformed shape, and the critical fracture location is accurately obtained.

Combining the deformed profile and the force–displacement curve in Fig. 12 (a, b), it is indicated that every peak force is corresponding to one fold-pair formation process. In both experiments and simulation, there are six fold-pairs formations in total, as marked on the deformed profile in Fig. 12 (a). The process stops before the sixth fold-pair formation ending as the total impact energy has already been absorbed. It shall be noted that force values measured from experiments are filtered at the early stage, hence, the second peak force is not observed in the experimental result. In terms of the deviation on the energy/force–displacement curves in Fig. 12 (b), the current material parameter set and the mesh of the FE model result in a slightly harder material behavior in the simulation. Referring to the specimen deformation contour figures, the crack initiation and propagation at both top edges and bending folds of the crash box specimen are well captured by the eMBW model, which are indicated with the orange arrows in Fig. 12 (c). In addition, with the simulation tool, the detailed performance of the material during the tube crushing test including the stress and strain distribution along deformation history as well as loading history of critical elements indicated crack mechanism can be analyzed in the following sections.

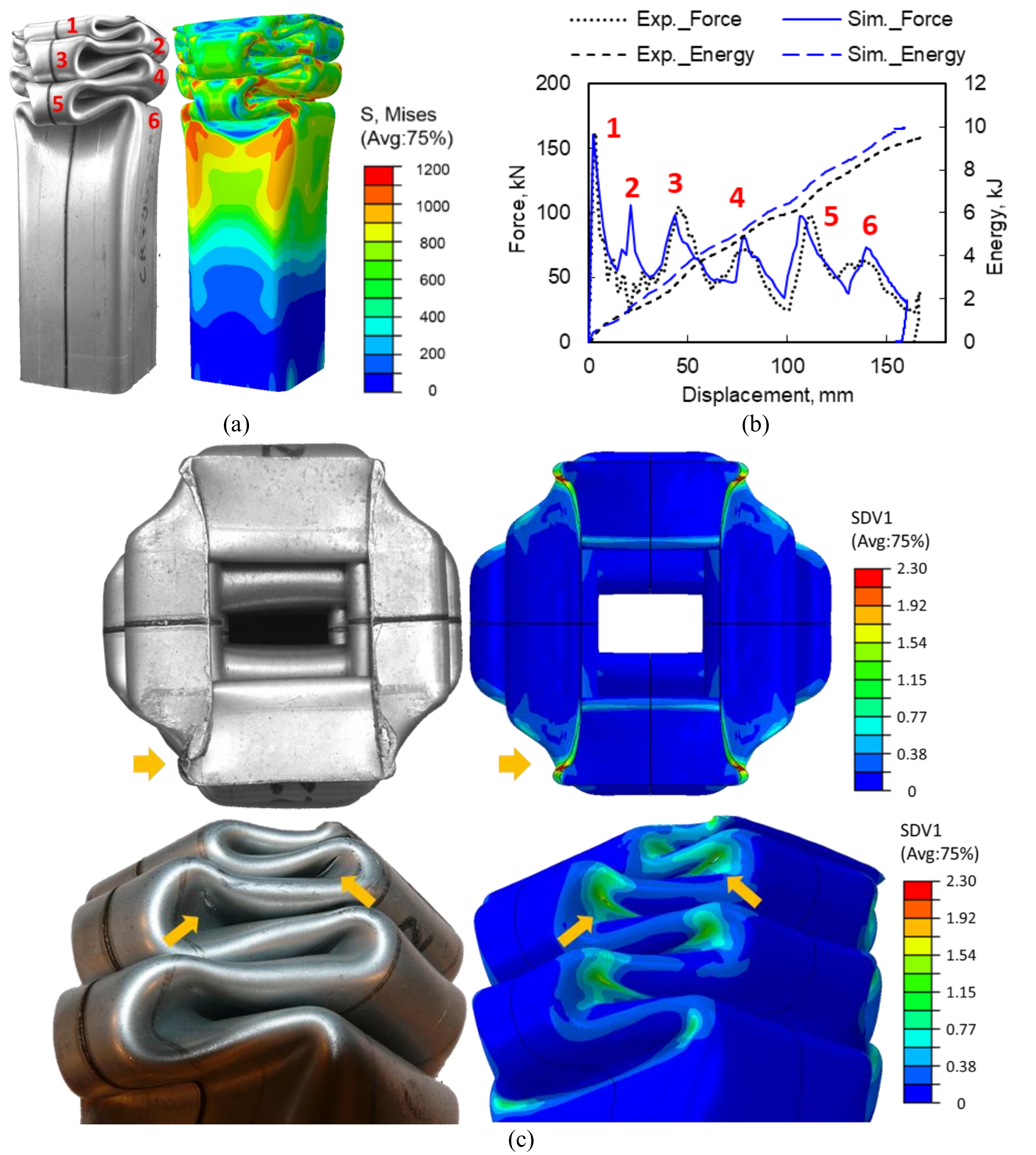

Fig. 12 Square tube crushing test simulation results. (a) Deformed profile and FE predicted result after impact; (b) Force/energy-displacement curves of experiment and simulation; (c) Crack investigation in deformed profile and FE prediction.

5.3 Discussion

5.3.1 Deformation history

As shown in Fig. 12 (a, b), it is illustrated that the peak force is related to the fold formation during the impact crushing deformation. Hence, the deformation patterns at every peak force moment from the simulation are plotted for the detailed understanding of the deformation history and folding mechanism. Fig. 13 shows the deformation contours in terms of the stress and strain fields referring to every peak force moment, indicated by the red numbers consistent with Fig. 12 (b). Here, the von Mises stress and the equivalent plastic strain (SDV1) are considered. The initial and final deformation states are also plotted as a reference.

The relationship between peak force and folding mechanism is revealed by combing the numbers in Fig. 12 (b) and Fig. 13 (a). Soon after the contact is established between the hammer and the square tube, the top edges on sidewalls with the pre-indentations is bent inwards. This bending leads to a first outward fold-pair formation at the very beginning of the crushing test, which forms at the same position with the pre-indentation but on the opposite welded sidewalls. The corresponding moment of the maximum crushing force is #1 in Fig. 13. It is clear to see that the moment is corresponding to the maximum bending moment for the structure. Then the second peak force occurs when the first fold-pair is completely bent meanwhile the secondary outward fold-pair is forming. The same force history can be explained for the following fold-pairs. The following fold-pair form alternatively on the subsequent opposite sidewalls in succession during the impact deformation. It can be concluded that the maximum crushing force is correlated to the formation of the fold with a small bending angle, and the minimum force is close to a formation of a fold in halfway. Furthermore, the strain field in Fig. 13 (b) reveals that the distinct plastic deformation happens in the folds and localizes at the pre-bending corners. That means the folds contribute mostly to the energy absorption, in particular, in the pre-bending corner part, which shows a relatively high equivalent plastic strain level up to 2.3. Besides, as most of the deformable areas go through the plastic strain lower than 0.5, the yielding strength and initial strain hardening are proved as the main contribution to the energy absorption during the tube crushing test. Therefore, to further improve the prediction quality, the manufacturing process by bending and indenting should also be considered in the future study to simulate the crushing process.

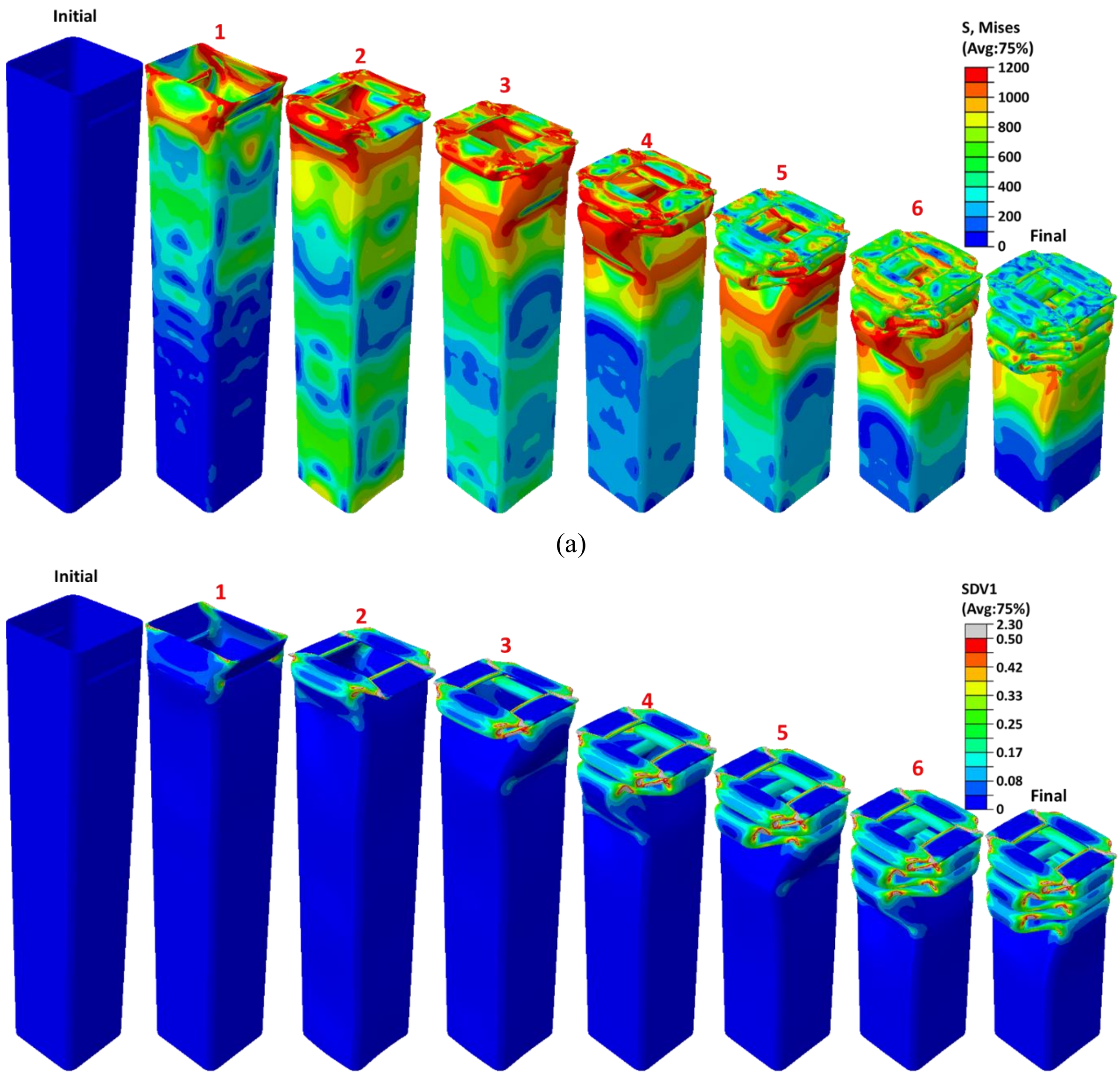

(a)

(b)

Fig. 13 The stress (a) and strain (b) field of crash box profile at the peak force moments. (SDV1 represents the equivalent plastic strain.)

5.3.2 Crack formation mechanics

To understand the crack formation mechanics, the large deformation zones are focused. After the test, there are three symmetrical crack zones in total, as indicated with numbers 1-3 in Fig. 14. Crack #1 locates on the top edge corners, while crack #2 and #3 are under the fold-pairs at the pre-bending zone. Fig. 14 gives the loading history analyses of the critical elements that finally are indicated as the first deleted element for a crack formation. If there are several elements vanishing at the same simulation interval, the element with the largest damage accumulation in the previous step is chosen as the critical element for this crack. It is illustrated that the stress states of the critical elements change severely with the impact loading.

The elements at the top corner (referring to crack #1) go through firstly a compression then a tension state. The final crack forms during tensile loading, corresponding to the tearing mode caused by the opposite folding deformation directions of neighboring elements. This is consistent with the experimental situation, as after the crushing sample contacting with the drop hammer plate, the material on one side of the corner is necked-in towards the inner crash box profile, while the material on the other side of the corner is forced to folding towards the outside surface of the profile. Therefore, the material on the top corner fails first. The average stress state of the critical element closes to the shear stress state. Besides, there are several neighboring elements that have reached a higher equivalent plastic strain value but are not deleted along the whole loading history as their stress triaxiality is lower than the critical stress triaxiality for damage or fracture occurrence. Therefore, to include the cut-off value of the crack initiation is critical for the correct fracture prediction in the tube crushing tests.

The transition between compression and tension state is also clear for the critical elements in the bending fold-pairs, such as crack #2 and #3. Furthermore, the absolute value of stress triaxiality is increased in general with further loading. It is notable that the final cracks always form under tensile states according to the average stress triaxiality values, and the cracks normally occur at the interior folding surfaces. It is counter-intuitive, as the elements at the interior bending surface shall experience compressive loading. The surprising change of the compression to tensile is caused by the second-level bending due to the self-contact with the previous fold, which finally triggers the crack formation during the square tube crushing.

For instance, crack #2 takes place under the second fold-pair and in the period between the third and fourth peak force, as shown in Fig. 14 (c).When the loading is imposed, this area is under the compression state firstly. Then it changes to the tension state rapidly caused by the first fold-pair formation, since the surface tension is necessary for the bending folds. However, during the forming process of the second and third fold-pairs, i.e. between the second and third peak force, it goes through the compression again due to its location. With the global deformation increasing, after the second fold-pair formation, the compressive force from the bent top edge is acting on this fold due to self-contact and inducing tensile bending again under the second fold-pair, indicated by the arrows in Fig. 14 (a). When the accumulated equivalent plastic strain reaches the critical ductile fracture strain according to the loading history, final crack initiation happens. Generally, for the critical element in the crack under the second fold (crack #2), the stress state is close to the plain-strain compression or tension condition during the whole deformation, as its Lode angle parameter changes around zero during the loading. The four distinct jumps in the stress triaxiality and Lode angle parameter indicate the forming of the previous four fold-pairs. The overall average stress state of the element at crack #2 is close to plane-strain tension condition as indicated by the dashed line in Fig. 14 (b).

A similar loading history can be seen for the critical element in the crack under the third fold-pair (crack #3). The difference is that as this element is far away from the impacting top, it first goes through the compression state during the formation of the first fold-pair. When the second fold-pair is forming, i.e. between the second and third peak forces, this element is under tension state due to the necessary surface tension for bending. Again, it goes back to the compression state at the formation period of third and fourth fold-pairs. Then the first fold compresses the third one and leads to the final crack initiation in the third fold-pair. A similar process can be imagined for more cracks initiation under the fold-pairs area if further deformation goes on, e.g. the second fold-pair will compress the fourth one and result in the crack formation, and so on. Therefore, the self-contact induced bending between the folds is the reason for crack initiation in the fold-pairs during the square tube crushing test.

In addition, it is also indicated that the fold cracks always initiate at one side close to the pre-bending corner, and then prorogate along the traversal direction to the sample center on the sample surface, which can be illustrated in the strain contour figure with cracks in the undeformed profile pattern (Fig. 15). That means if the fold cracks occur, they will be locally limited within the fold zones. The strain localization areas close to the pre-bending corner are also clearly investigated in Fig. 15.

Overall, the application of the uncoupled eMBW model shows a good performance on the square tube crushing test simulation. The main material behavior during the crushing test can be well captured and further investigated in the numerical simulation approach, which is helpful for understanding the deformation and crack initiation mechanics in square tube crushing and the future material design for the crash box component. It shall be emphasized that the current prediction is based on the assumption that the damage and fracture are independent of strain rates and temperature, which appears to produce reasonably well results in the crushing tests. However, a systematic investigation is needed to describe the ductile failure in the 3D domain of temperature, strain rate, and stress state. In addition, regarding the final crack size, the FE simulation should be further improved in terms of the mesh size and material parameters. It is also noted that due to the one-quarter symmetry in the FE model, the deformation behavior in simulation is totally the same for each one-quarter specimen part, while in the experiment, the deformation pattern could be slightly different in each one-quarter specimen part, e.g. the cracks at the top corners. For a better prediction, a full model should be considered. In order to balance the model prediction performance and computational capability, the non-local formulation of the eMBW model [61], which can account for the strain gradient effect, will be taken into account in the future study to minimize the mesh size effect on the local deformation and fracture behavior.

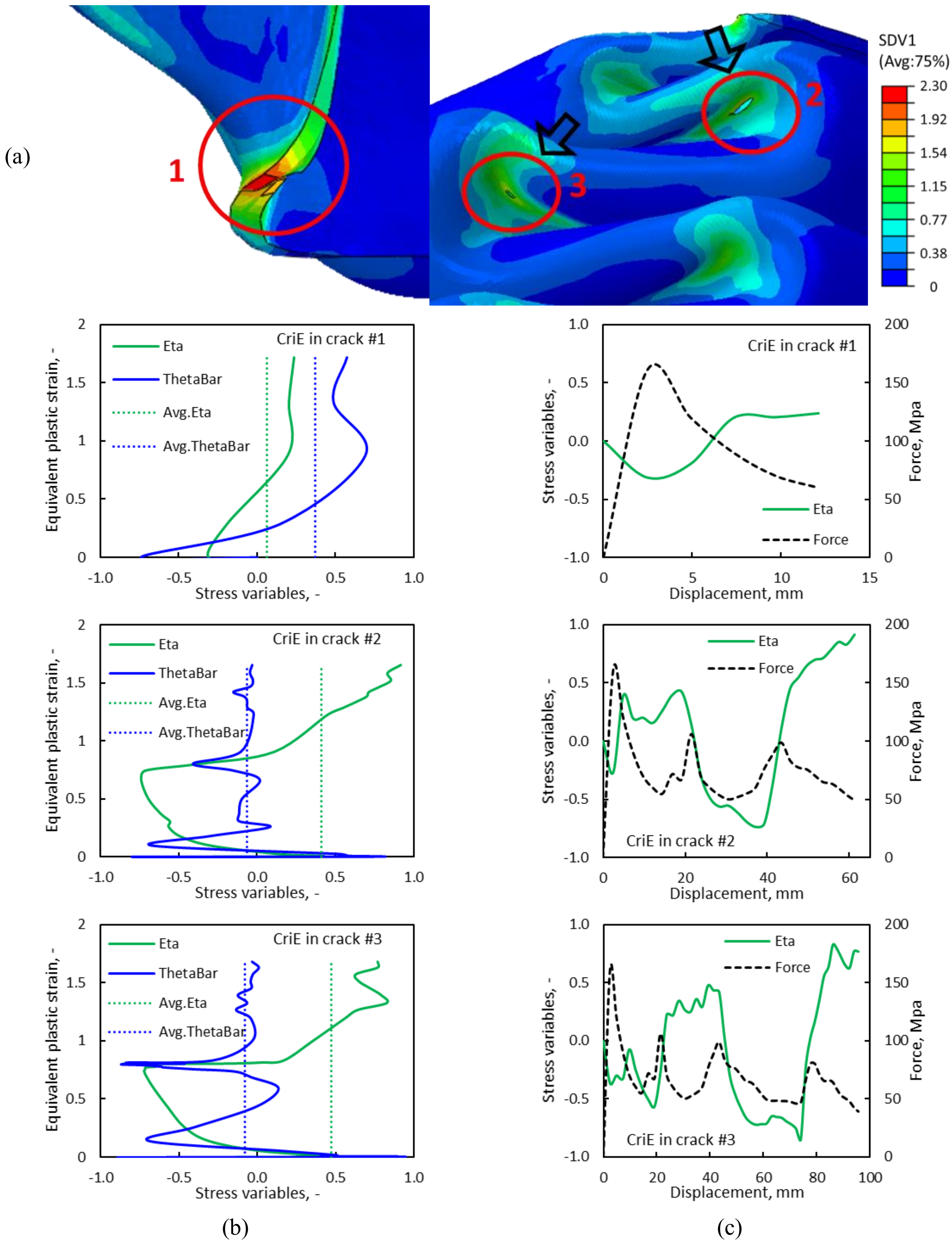

Fig. 14 Investigation of the crack formation mechanics during the square tube crushing test. (a) Location of cracks. (b) Loading history of the critical elements in the cracks zone. (c) Stress states of critical elements related to the force–displacement moments.

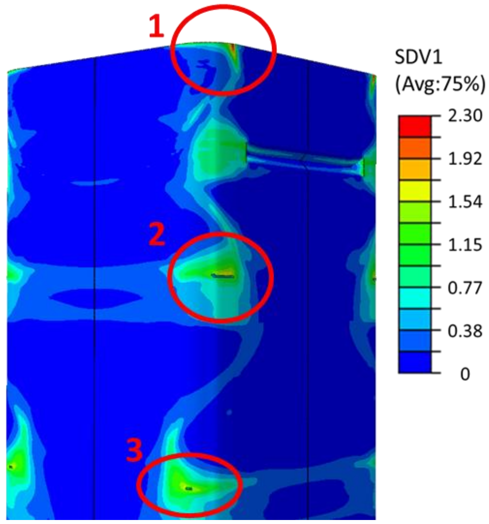

Fig. 15 The strain field with cracks of crushing square tube in the undeformed pattern.

6 Conclusions

- An experimental and numerical program is conducted to characterize the plasticity and failure behavior with various temperatures, strain rates, and stress states of DP1000 steel sheets.
- A method to calibrate the Taylor–Quinney coefficient and calculate the adiabatic heating effect during plastic deformation at the intermediate strain rate regime is proposed. With the proposed method, the iso-thermal stress–strain curves at the transition and high strain rate regimes can be calculated.
- The hybrid damage mechanics model is extended to consider the effects of temperature, strain rate, and loading history on material mechanical properties. A complete material parameter calibration program based on the lab tests is presented and the model successfully predicts the crashworthiness properties (force–displacement response, energy dissipation, deformation profile, and crack formation) of the dynamic square tube crushing test at the structure scale.
- For the investigated high-strength DP1000 steel sheets, short cracks at the folds are found during the dynamic square tube crushing tests. The formation of these short cracks is accurately predicted by the proposed model. It is concluded that the consideration of the stress state history on damage accumulation and the cut-off value of failure is critical for accurate prediction.
- The detailed stress state history of the hotspots during the crushing loading of the square tube is analyzed in the investigation. Very complicated loading history across compression, shear, and tension is found. Two types of crack formation mechanics are identified: shearing and second-level bending caused by the self-contact between the formed folds.

Acknowledgments

The authors gratefully acknowledge the European Commission Research Fund for Coal and Steel (RFCS) [grant number: 709711] for the financial funding for the project. We also gratefully acknowledge Dr. Helmut Richter and Dr. Thomas Pretorius from Technology & Innovation (TIS) of thyssenkrupp Steel Europe AG (tkSE) for material supply and the impact tests. JL would like to thank Professor Tomasz Wierzbicki at MIT for valuable discussion on the deformation and crack mechanics on the tube crushing tests. Simulations were performed with computing resources granted by RWTH Aachen University under project rwth0237.

References

[1] J. Fang, G. Sun, N. Qiu, N.H. Kim, Q. Li, On design optimization for structural crashworthiness and its state of the art, Structural and Multidisciplinary Optimization, 55 (2017) 1091-1119.

[2] A. Baroutaji, M. Sajjia, A.-G. Olabi, On the crashworthiness performance of thin-walled energy absorbers: Recent advances and future developments, Thin Walled Struct., 118 (2017) 137-163.

[3] F. Xu, X. Zhang, H. Zhang, A review on functionally graded structures and materials for energy absorption, Eng. Struct., 171 (2018) 309-325.

[4] T. Wierzbicki, Crushing analysis of metal honeycombs, Int. J. Impact Eng., 1 (1983) 157-174.

[5] W. Abramowicz, The effective crushing distance in axially compressed thin-walled metal columns, Int. J. Impact Eng., 1 (1983) 309-317.

[6] T. Wierzbicki, W. Abramowicz, On the Crushing Mechanics of Thin-Walled Structures, J. Appl. Mech., 50 (1983) 727-734.

[7] W. Abramowicz, T. Wierzbicki, Axial Crushing of Multicorner Sheet Metal Columns, J. Appl. Mech., 56 (1989) 113-120.

[8] W. Abramowicz, N. Jones, Dynamic axial crushing of square tubes, Int. J. Impact Eng., 2 (1984) 179-208.

[9] W. Abramowicz, N. Jones, Dynamic axial crushing of circular tubes, Int. J. Impact Eng., 2 (1984) 263-281.

[10] W. Abramowicz, N. Jones, Dynamic progressive buckling of circular and square tubes, Int. J. Impact Eng., 4 (1986) 243-270.

[11] T. Wierzbicki, L. Recke, W. Abramowicz, T. Gholami, Stress profiles in thin-walled prismatic columns subjected to crush loading - I. Compression, Computers & Structures, 51 (1994) 611-623.

[12] T. Wierzbicki, L. Recke, W. Abramowicz, T. Gholami, J. Huang, Stress profiles in thin-walled prismatic columns subjected to crush loading - II. Bending, Computers & Structures, 51 (1994) 625-641.

[13] A. Otubushin, Detailed validation of a non-linear finite element code using dynamic axial crushing of a square tube, Int. J. Impact Eng., 21 (1998) 349-368.

[14] G. Sun, T. Pang, C. Xu, G. Zheng, J. Song, Energy absorption mechanics for variable thickness thin-walled structures, Thin Walled Struct., 118 (2017) 214-228.

[15] G. Li, F. Xu, G. Sun, Q. Li, A comparative study on thin-walled structures with functionally graded thickness (FGT) and tapered tubes withstanding oblique impact loading, International Journal of Impact Engineering, 77 (2015) 68-83.

[16] H. Zhang, G. Sun, Z. Xiao, G. Li, Q. Li, Bending characteristics of top-hat structures through tailor rolled blank (TRB) process, Thin-Walled Structures, 123 (2018) 420-440.

[17] M. Bambach, L. Conrads, M. Daamen, O. Güvenç, G. Hirt, Enhancing the crashworthiness of high-manganese steel by strain-hardening engineering, and tailored folding by local heat-treatment, Materials & Design, 110 (2016) 157-168.
[18] C.P. Kohar, M. Mohammadi, R.K. Mishra, K. Inal, Effects of elastic–plastic behaviour on the axial crush response of square tubes, Thin Walled Struct., 93 (2015) 64-87.
[19] H. Gedikli, Numerical investigation of axial crushing behavior of a tailor welded tube, Materials & Design, 44 (2013) 587-595.
[20] J. Fu, Q. Liu, K. Liufu, Y. Deng, J. Fang, Q. Li, Design of bionic-bamboo thin-walled structures for energy absorption, Thin-Walled Structures, 135 (2019) 400-413.
[21] Y.B. Bao, T. Wierzbicki, On fracture locus in the equivalent strain and stress triaxiality space, Int. J. Mech. Sci., 46 (2004) 81-98.
[22] Y. Bao, T. Wierzbicki, A Comparative Study on Various Ductile Crack Formation Criteria, Journal of Engineering Materials and Technology, 126 (2004) 314-324.
[23] Y.L. Bai, T. Wierzbicki, A new model of metal plasticity and fracture with pressure and Lode dependence, Int. J. Plasticity, 24 (2008) 1071-1096.
[24] L. Xue, T. Wierzbicki, Ductile fracture initiation and propagation modeling using damage plasticity theory, Engineering Fracture Mechanics, 75 (2008) 3276-3293.
[25] S.J. Marcadet, D. Mohr, Effect of compression–tension loading reversal on the strain to fracture of dual phase steel sheets, Int. J. Plasticity, 72 (2015) 21-43.
[26] S.J. Marcadet, D. Mohr, Critical hardening rate model for predicting path-dependent ductile fracture, Int. J. Fract., 200 (2016) 77-98.
[27] C.C. Roth, D. Mohr, Effect of strain rate on ductile fracture initiation in advanced high strength steel sheets: Experiments and modeling, Int. J. Plasticity, 56 (2014) 19-44.
[28] J. He, J. Lian, G. Golisch, A. He, Y. Di, S. Münstermann, Investigation on micromechanism and stress state effects on cleavage fracture of ferritic-pearlitic steel at −196°C, Materials Science and Engineering: A, 686 (2017) 134-141.
[29] A.S. Khan, H.W. Liu, Strain rate and temperature dependent fracture criteria for isotropic and anisotropic metals, Int. J. Plasticity, 37 (2012) 1-15.
[30] B. Erice, F. Galvez, D.A. Cendon, V. Sanchez-Galvez, Flow and fracture behaviour of FV535 steel at different triaxialities, strain rates and temperatures, Engineering Fracture Mechanics, 79 (2012) 1-17.
[31] D. Lassance, D. Fabregue, F. Delannay, T. Pardoen, Micromechanics of room and high temperature fracture in 6xxx Al alloys, Prog. Mater Sci., 52 (2007) 62-129.
[32] D. Mohr, S.J. Marcadet, Micromechanically-motivated phenomenological Hosford–Coulomb model for predicting ductile fracture initiation at low stress triaxialities, Int. J. Solids Struct., 67-68 (2015) 40-55.

[33] T.B. Stoughton, J.W. Yoon, A new approach for failure criterion for sheet metals, Int. J. Plasticity, 27 (2011) 440-459.
[34] M. Gorji, B. Berisha, P. Hora, F. Barlat, Modeling of localization and fracture phenomena in strain and stress space for sheet metal forming, Int. J. Mater. Form., 9 (2016) 573-584.
[35] N. Park, H. Huh, S.J. Lim, Y. Lou, Y.S. Kang, M.H. Seo, Fracture-based forming limit criteria for anisotropic materials in sheet metal forming, Int. J. Plasticity, 96 (2017) 1-35.
[36] Q. Hu, X. Li, X. Han, J. Chen, A new shear and tension based ductile fracture criterion: Modeling and validation, Eur. J. Mech. A. Solids, 66 (2017) 370-386.
[37] Y. Lou, J.W. Yoon, H. Huh, Modeling of shear ductile fracture considering a changeable cut-off value for stress triaxiality, Int. J. Plasticity, 54 (2014) 56-80.
[38] Y.L. Bai, T. Wierzbicki, A comparative study of three groups of ductile fracture loci in the 3D space, Engineering Fracture Mechanics, 135 (2015) 147-167.
[39] T. Wierzbicki, Y. Bao, Y.-W. Lee, Y. Bai, Calibration and evaluation of seven fracture models, Int. J. Mech. Sci., 47 (2005) 719-743.
[40] J. Lian, T. Wierzbicki, J. Zhu, W. Li, Prediction of shear crack formation of lithium-ion batteries under rod indentation: Comparison of seven failure criteria, Engineering Fracture Mechanics, 217 (2019) 106520.
[41] A.L. Gurson, Continuum theory of ductile rupture by void nucleation and growth: Part I–yield criteria and flow rules for porous ductile media, J. Eng. Mater. Technol.-Trans. ASME, 99 (1977) 2-15.
[42] V. Tvergaard, On localization in ductile materials containing spherical voids, Int. J. Fract., 18 (1982) 237-252.
[43] V. Tvergaard, A. Needleman, Analysis of the cup-cone fracture in a round tensile bar, Acta Metall., 32 (1984) 157-169.
[44] J. Lemaitre, A continuous damage mechanics model for ductile fracture, J. Eng. Mater. Technol.-Trans. ASME, 107 (1985) 83-89.
[45] Y. Shinohara, Y. Madi, J. Besson, Anisotropic ductile failure of a high-strength line pipe steel, Int. J. Fract., 197 (2016) 127-145.
[46] A. Seupel, M. Kuna, A gradient-enhanced damage model motivated by engineering approaches to ductile failure of steels, Int. J. Damage Mech., 28 (2019) 1261-1296.
[47] Z. Yue, K. Cao, H. Badreddine, K. Saanouni, J. Gao, Failure prediction on steel sheet under different loading paths based on fully coupled ductile damage model, Int. J. Mech. Sci., 153-154 (2019) 1-9.
[48] J. Lian, M. Sharaf, F. Archie, S. Münstermann, A hybrid approach for modelling of plasticity and failure behaviour of advanced high-strength steel sheets, Int. J. Damage Mech., 22 (2013) 188-218.
[49] J. Lian, J. Wu, S. Muenstermann, Evaluation of the cold formability of high-strength low-alloy steel plates with the modified Bai-Wierzbicki damage model, Int. J. Damage Mech., 24 (2015) 383-417.

[50] J. Lian, P. Liu, S. Münstermann, Modeling of damage and failure of dual phase steel in Nakajima test, Key Eng. Mater., 525-526 (2012) 69-72.
[51] D. Novokshanov, B. Döbereiner, M. Sharaf, S. Münstermann, J. Lian, A new model for upper shelf impact toughness assessment with a computationally efficient parameter identification algorithm, Engineering Fracture Mechanics, 148 (2015) 281-303.
[52] S. Münstermann, C. Schruff, J. Lian, B. Dobereiner, V. Brinnel, B. Wu, Predicting lower bound damage curves for high-strength low-alloy steels, Fatigue & Fracture of Engineering Materials & Structures, 36 (2013) 779-794.
[53] B. Wu, X. Li, Y. Di, V. Brinnel, J. Lian, S. Münstermann, Extension of the modified Bai-Wierzbicki model for predicting ductile fracture under complex loading conditions, Fatigue & Fracture of Engineering Materials & Structures, 40 (2017) 2152-2168.
[54] J. Lian, S. Münstermann, W. Bleck, Damage and fracture loci for a dual-phase steel and a high-strength low-alloyed steel: Revealing the different plastic localization–damage–ductile fracture pattern, AIP Conference Proceedings, 1769 (2016) 200020.
[55] W. Liu, J. Lian, S. Münstermann, Damage mechanism analysis of a high-strength dual-phase steel sheet with optimized fracture samples for various stress states and loading rates, Eng. Fail. Anal., 106 (2019) 104138.
[56] W. Liu, J. Lian, N. Aravas, S. Münstermann, A strategy for synthetic microstructure generation and crystal plasticity parameter calibration of fine-grain-structured dual-phase steel, Int. J. Plasticity, in press (2019).
[57] Metallic materials. Tensile testing. Method of test at room temperature, in, British Standards Institution, London, 2016, pp. 88.
[58] X. Fang, R. Grams, A Novel Oscillation-Free Force Measurement for the Determination of Material Properties during High-Speed Tests, (2021).
[59] S. Farren William, I. Taylor Geoffrey, The heat developed during plastic extension of metals, Proceedings of the Royal Society of London. Series A, Containing Papers of a Mathematical and Physical Character, 107 (1925) 422-451.
[60] I. Taylor Geoffrey, H. Quinney, The latent energy remaining in a metal after cold working, Proceedings of the Royal Society of London. Series A, Containing Papers of a Mathematical and Physical Character, 143 (1934) 307-326.
[61] I. Papadioti, N. Aravas, J. Lian, S. Münstermann, A strain-gradient isotropic elastoplastic damage model with J3 dependence, Int. J. Solids Struct., 174-175 (2019) 98-127.